

Impact of transient fluctuations on proton beams in its space-charge-dominated regime: *Measurement-based stochastic noise model of low- γ synchrotron*

Phil S. Yoon

^a Fermi National Accelerator Laboratory, Batavia, IL 60510, U.S.A.

^b Department of Physics and Astronomy, University of Rochester, Rochester, NY 14620, U.S.A.

Abstract

Transient electric-current fluctuations arising from magnet power supplies can be translated into magnetic-field perturbations during particle-accelerator operations. As speculated over the past decades, this type of inevitable machine imperfection can lead to emittance growths, halo formation, and consequential beam losses. With robust experimental evidence of transient coloured noise from the power supplies and its real-time Fast-Fourier-Transform analysis, the ripple currents were modelled on the Ornstein-Uhlenbeck process via parameterisation. For investigating the conjectured effects on intense beams, the first-ever stochastic noise model—equipped with the wide-spectrum noise generator and a suite of beam-diagnostic calculations—was formulated with realism by enabling beams to propagate through focusing channels in the face of power-supply ripples and space charge. It is concluded that fluctuating power-supply currents, when coupled to space charge and impinging upon intense proton beams, can substantially escalate the insidious process of degrading beam properties during the full injection period. This article concerns the systematised methodology of constructing a hybrid of empirical and numerical models for quantitatively assessing the impact of frequency-dependent noise on beams and the attendant ramifications engendered in its space-charge-dominated regime.

Keywords: accelerator physics; accelerator modelling; beam injection; Brownian motion; charged-particle beams; fluctuation phenomena; Langevin method; nonlinear dynamics; power supply; space charge; stochastic noise; synchrotrons

1. INTRODUCTION

Subtle and transient fluctuations are inevitable and ubiquitous in a wide variety of problems in nature: *e.g.*, operation of particle accelerators, stellar dynamics, climate changes, colloid chemistry to name a few. To start out, an ensemble of charged particles is defined as *the system*, and all the beamline components—*e.g.*, radio-frequency (RF) cavities, magnets, power supplies, beam-diagnostic devices, etc.—designed for accelerating, guiding, and diagnosing particle beams as *the surroundings* that interact closely with the system. Charged-particle beams (*beams* hereafter) identify the surroundings of beamline components as sources of transient noise, as illustrated by Figure 1. Intrinsic to particle accelerators of all types is external noise caused by unavoidable machine imperfections, or environmental disturbances of terrestrial, anthropogenic, or electric origin: *e.g.*, earthquakes, ground vibration motions, traffic noise on surface ground in the vicinity, and ripple currents coming from power

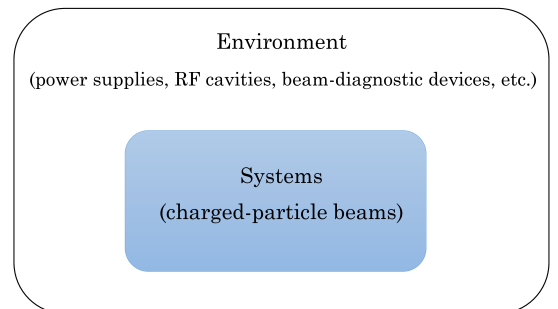


Figure 1 | The system and the surroundings defined for modelling a particle-accelerator system.

supplies. Motivated by prior findings from simplified, theoretical models of coloured noise[1, 2], it had been conjectured that the adverse influence of fluctuating electric currents (*the ripples* hereafter) originating from the magnet power supplies accounts possibly for the conspicuous phenomenon of beam losses plaguing during the injection period of the Booster synchrotron (*the Booster* hereafter). The pernicious occurrence of sapping proton beams of their intensities raised a serious con-

Email address: phil.s.yoon@gmail.com (Phil S. Yoon)

cern for the fixed-target experiments relying upon sorely needed intense proton beams from the Booster[?]. Hence, this stochastic noise model was developed to investigate this uncanny phenomenon, of which emergence was hypothesised to be from potential ripples of power supplies of the low- γ synchrotron.

2. MODELLING METHODOLOGY

The growing need to investigate the harmful effects, which power-supply current fluctuations is speculated to have on beams, had left strong motivation for constructing a stochastic noise model. At first, a potent and efficient numerical algorithm was developed; this algorithm employing the Box-Muller-like transformation can generate a wide spectrum of parameterised stochastic noise by harnessing the Ornstein-Uhlenbeck (O-U) process[4] that a Langevin-like stochastic differential equation governs[5](sec. 6.2).

This new noise module, in turn, dovetails with the framework of the pre-existing Objective Ring Beam Injection and Tracking (ORBIT) simulation package[?]. Prior to experimental measurements, we simulated the degrading effects on proton beams propagating through periodic focusing channels under space-charge effects by adding the O-U noise with differing strengths. Our interest was sparked when the results from the preliminary noise model corroborated the adverse effects of external fluctuations. Moreover, our preliminary findings are consistent with earlier findings from the theoretical model of collective space-charge modes coupled with dynamic noise[1, 2]. With confirmation supplied by the preliminary model, we proceeded to devise experimental methods for directly measuring common-/differential-mode voltages and minute transients in the power-supply electric currents. The real-time Fourier analysis of data sampled from each individual power supplies verified the presence of substantial time-dependent stochastic fluctuations that can transmit through the magnet circuitry. Moreover, equivalent-circuit simulations were checked to see if there exist resonances around the magnet circuitry. Based upon the results of the computationally efficient Fast-Fourier-Transform of the measured current ripples, its stochastic parameterisation was performed by matching the power-spectral densities (PSDs) between the measured ripples and the simulated noise[4]. By translating modelled O-U noise into induced magnetic-field undulations, tracking huge herds of macroparticles (simulation particles) was reiterated under the influence of three dimen-

sional (3-D) space-charge forces. The following Figure 2 and Figure 3 illustrate the multistage approach to modelling current ripples and their influence on beams. For parameterising the stochastic ripples, the experimental *signature space* mapped on to the stochastic *parameter space*; in this process, great care was taken to tune faithfully up the model on the data of the power-supply ripples. Consequently, the technique of Fast-Fourier-Transform (FFT) enabled matching the power-spectral density of the measured ripple currents to that of the simulated O-U noise.

3. NOISE-MEASURING TECHNIQUES AND ANALYSIS

This section is devoted to techniques of measuring and analysing transient coloured noise echoing around the magnet power system.

3.1. Common- and Differential-Mode Noise

Sampling 15-Hz current waveforms on the main bus line (Figure 4) and measuring common-mode (CM) and differential-mode (DM) voltages (Figure 6) together were conducted at each respective GMPS units. It was confirmed by a series of measurements that ripple currents and CM voltages have been consistently detected and thus are not of seasonal behaviour appearing at each GMPS unit (Supplementary Figure 1). CM and DM voltages were computed in *real time* on the digital oscilloscope as follows:

$$\begin{cases} V_{CM} = V_{+G} + V_{-G} \\ V_{DM} = V_{+G} - V_{-G} \end{cases} \quad (1)$$

The waveforms of V_{+G} and the inverted V_{-G} (\tilde{V}_{-G}) were overlaid for easy comparison on the same scale in Supplementary Figure 1. In addition, overlaid CM voltages were graphed against V_{+G} and \tilde{V}_{-G} for each respective GMPS (Supplementary Figure 2). Potential differentials are shown in Supplementary Figure 3. DM voltages are shown in Supplementary Figure 4. The DC output of the power supply was filtered with a L - C network, with the aid of a 15-Hz low-pass filter, in order to smooth the differential-mode sawtooth waveforms at all GMPS units. The waveforms of CM voltage V_{CM} are noticeably fast fluctuating, thereby inducing additional current fluctuations in the system. Peak-to-peak amplitudes of V_{+G} and \tilde{V}_{-G} are compared in Supplementary Figure 3, whereas phase lags between waveforms

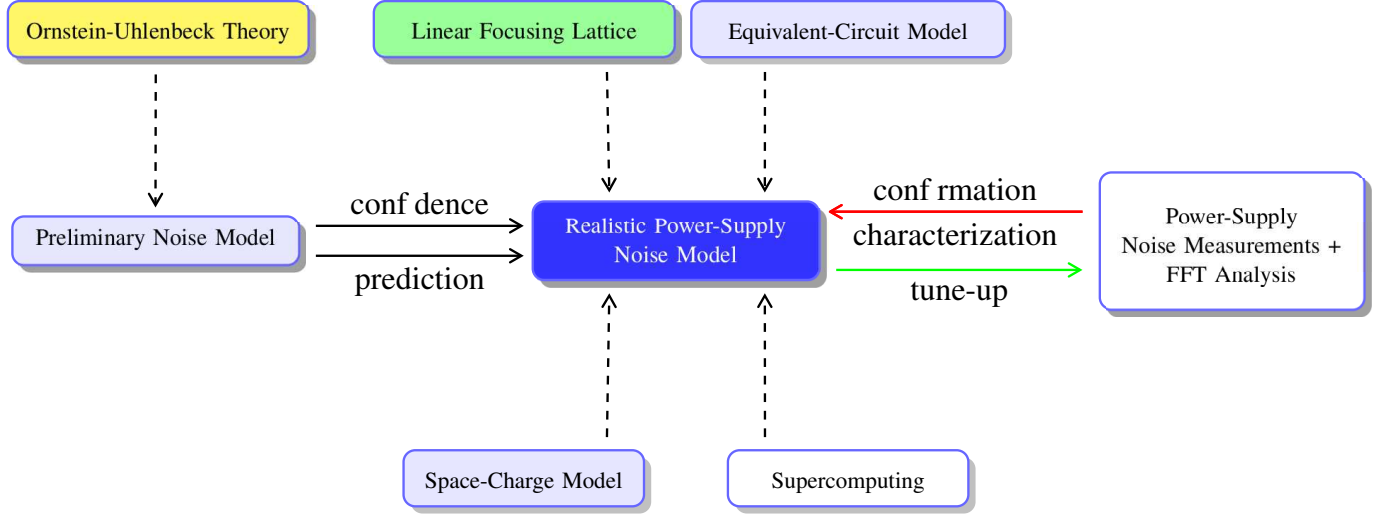


Figure 2 | Block diagram illustrating the multistage approach taken to modelling the influence of power-supply noise on intense charged-particle beams.

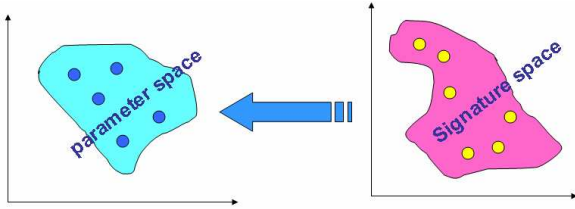


Figure 3 | Mapping the experimental signature space on to the stochastic parameter space.

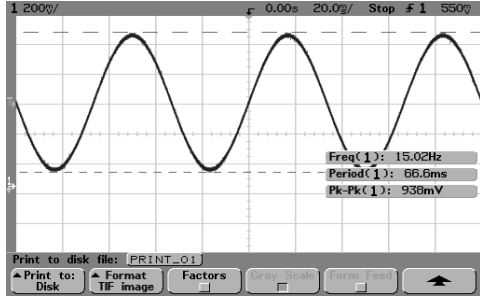


Figure 4 | Current waveform of 15 Hz taken at GMPS [1]. Its frequency and period are displayed in the background.

of V_{+G} and \tilde{V}_{-G} in Supplementary Figure 5. A campaign of measurements has found that a varying measure of mismatches between potential differentials and phase lags in V_{+G} and V_{-G} comes into existence at each individual GMPS unit. The following are the two root causes of the common-mode noise arising from each GMPS unit: (1) additional phase lags ΔX in V_{+G} and V_{-G} and (2) potential differentials between V_{+G} and \tilde{V}_{-G} . When V_{+G} and V_{-G} are added in a point-by-point fashion on the scope, they do not cancel out each other. Rather, the ripples



Figure 5 | A tandem of the GMPS units stand side by side in the East Booster Gallery. The waveforms of both V_{+G} and V_{-G} signals (Figure 6) were sampled directly from the GMPS control rack seen on the front chassis.

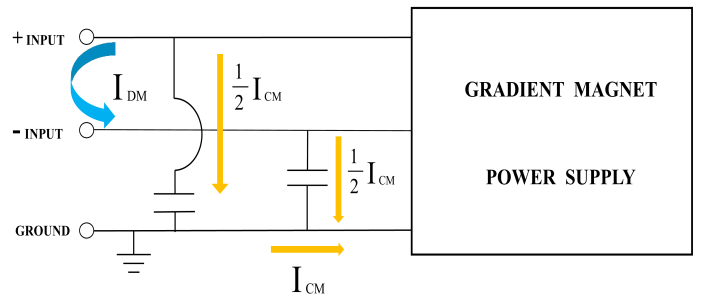


Figure 6 | Common- and differential-mode currents sampled from each of the GMPS units.

on each waveform add up, and thus the common-mode voltage stands out. The potential differentials and the phase lags measured for individual GMPS units are summarized in Table 1. As found, the fractional potential differential of GMPS [2] is amongst the greatest. Since the magnitude of the ripples is such

Table 1 | Differentials of voltage amplitudes (ΔV) and phase lags (ΔX) between V_{+G} and V_{-G} at each respective GMPS unit.

GMPS [No.]	V_{+G} (V)	V_{-G} (V)	$ \Delta V/V_{+G} $	ΔX (ms)
GMPS [1]	1.577	1.905	20.8 %	0.6
GMPS [2]	3.232	1.699	47.4 %	4.0
GMPS [3]	1.598	1.740	8.90 %	1.4
GMPS [4]	1.581	1.743	10.2 %	4.6

a small fraction of that of the baseline current, transducer electronics and a current amplifier (TA22 Texas Instruments) were utilised for amplifying signals. FFT impulses of the current waveform of one cycle are displayed in Figure 9.

3.2. Power Spectral Density: FFT Analysis

Common-mode voltages and current ripples rising above baseline current signals measured at the four GMPS units are Fourier-analyzed in real time. Evidencing the existence of the offending interferences stemming from the power-supply system required all the signals to be analyzed in *real time*. For this purpose, *real-time analysis* was conducted with the aid of the built-in FFT-function available on the scope.

3.3. Parameterisation of Power-Supply Ripples

The autocorrelation time τ_{ac} can be thought of as a memory span, or a measure of the dependence of the same stochastic value at two distinct times (t and t'). In this subsection, the measured current fluctuations were parameterised with a set of three stochastic quantities that follows:

- (1) **time step Δt** : The Booster's entire magnet system is divided into four quadrants, each of which constitutes a string of 24 magnets in series connection. And each of the four power-supply units drives its corresponding quadrant. Current fluctuations $\Delta I/I$ stemming from each GMPS are transmissive through a string of magnets contained in each quadrant. As such, all of the 24 magnets undergo the same amount of ripple currents at an interval of the time step. Thus, time step, or noise-sampling rate was chosen to be one revolution period ($T_0 = 2.2 \mu s$) at an injection energy of 400 MeV.
- (2) **autocorrelation time τ_{ac}** : On the basis of direct current measurements from a main bus line, the ripples are repeated above the baseline current, or reference current at an interval of $1.5 \sim 1.7$ (ms) (Figure 7). Therefore, a span of 1.5

~ 1.7 (ms) is elected to be the proper autocorrelation time for current fluctuations originating from the GMPS units.

- (3) **noise strength \mathcal{A}** : Based upon the fractional ripple currents $\Delta I/I$ subsisting on a linear-ramp segment of a sinusoidal current waveform (Figure 7), the r.m.s. value of fractional current fluctuations $\Delta I/I|_{rms}$ is on the order of 10^{-4} . For the verification purpose, histograms of the O-U noise generated at each noise node symmetrically inserted within the Booster model are shown in Figure 8. The r.m.s. values of histograms remain on the same order, as those of measured noise strengths.

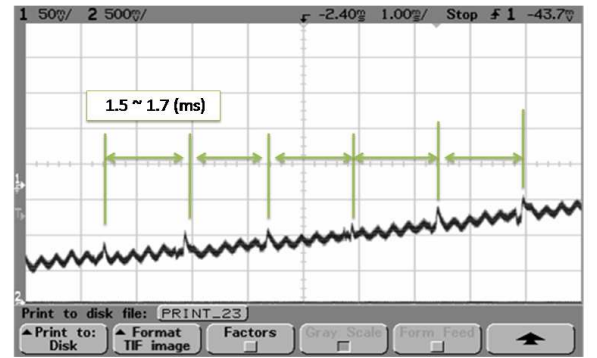


Figure 7 | Ripples rising above a linear segment of a sinusoidal current waveform. The current waveforms were sampled directly from the magnet bus line.

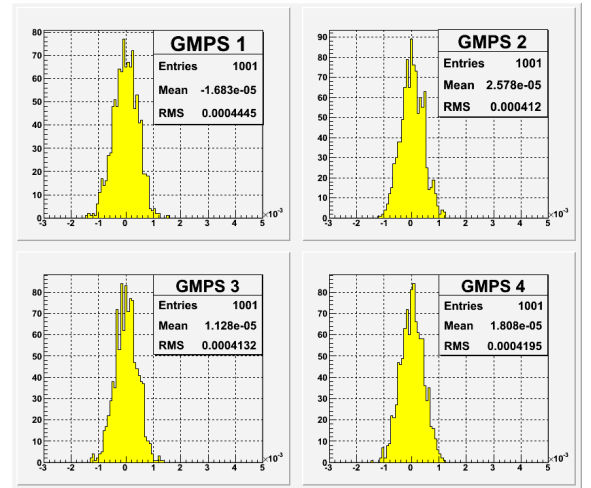
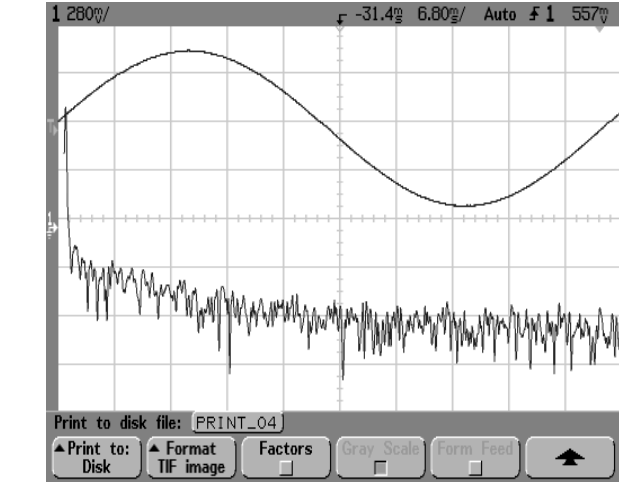


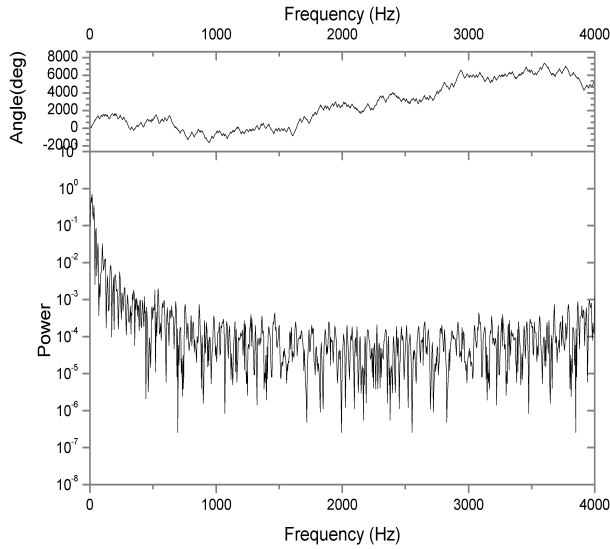
Figure 8 | Histograms of noise amplitudes generated at four random-noise nodes established within the stochastic noise model. Each noise node represents its associated GMPS unit within the model.

The FFT analysis of the acquired 15-Hz currents was performed over one-period range. The power spectral density of the sim-

ulated O-U noise was matched closely to that of the measured ripple currents (Figure 9).



(a) measured ripple currents



(b) simulated Ornstein-Uhlenbeck noise

Figure 9 | (a) Shown above are FFT impulses and a 15-Hz current waveform of one cycle; the horizontal scale is set to 167 Hz/div and the vertical scale to 20 dB/div. (b) The vertical scale is 10^{-1} /div to indicate power attenuations from unity.

3.4. Equivalent-Circuit Model

Equivalent-circuit modelling was carried out to find out the existence of offending resonances, acting as *noise amplifiers*, whilst reverberating through the magnet system. The SPICE (B² SPICE [19], A/D Version 4) model of one single LC-resonant cell is drawn in Figure 10[18]. A string of 24 magnets are operating in each quadrant. As such, those magnets in series connection can be

treated as a single transmission line. The results of AC analysis of the equivalent circuits are shown in Figure 11. The current is peaked at 15 Hz and a cluster of minor peaks are accompanied in a few kHz range. Our interpretation is that those offending resonances above 15 Hz in the higher frequency band can possibly amplify the power-supply noise, when the noise frequencies coincide with resonance frequencies. As a result, the existent resonances could accentuate the formation of beam halos, leading to pronounced beam losses incurred throughout the full injection cycle.

4. NOISE CLASSIFICATION AND CHARACTERISATION

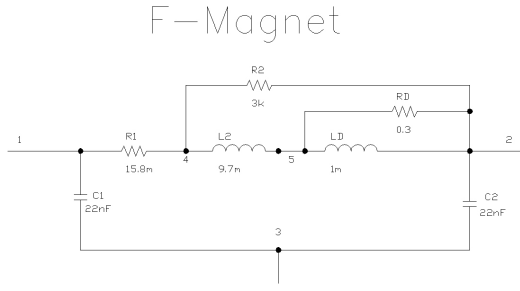
In the preceding section, the measuring techniques we devised have confirmed and provided robust evidence for the actuality of frequency-dependent stochastic noise arising from magnet's power system. In general, noise can be categorised broadly into two types: *i.e.*, *external* and *internal noise*. This stochastic noise model takes the ripple currents coming from the power supplies as external fluctuations impinging upon proton beams sourced from the Booster (Figure 1).

4.1. External Noise

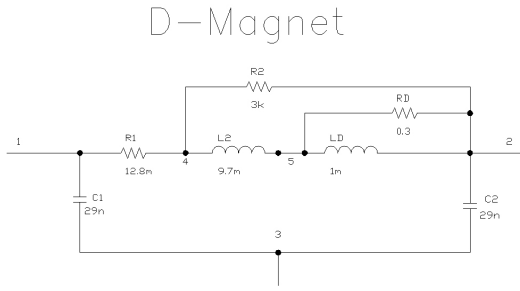
External noise is originated from a source outside of the system; *i.e.*, beamline components. Since the effects of external noise can be described by a stochastic differential equation (SDE) we opted for Langevin Equation (*LE* hereafter) for current fluctuations arising from power supplies. It is worth noting that the power-supply ripples are considered *indeterministic*, *stochastic*, or *aperiodic* in the sense that the occurrence of such current fluctuations never repeat themselves in an exact manner.

4.2. Electromagnetic Interferences

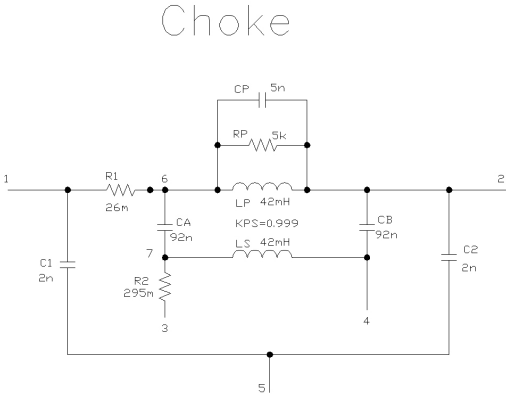
Electromagnetic Interference (EMI) noise[7, 8] results from rapid changes in voltage and current in electronic systems. And transmission of EMI noise is characterised as either *radiative*, or *conductive*. Conductive EMI noise—such as common-mode and differential-mode noise—is usually several orders of magnitude more copious than the radiative EMI, and thus can be more detrimental to the system. Given impedance $Z(\omega)$ as a function of frequency ω , fluctuations in common-mode voltage V_{CM} induce common-mode currents I_{CM} , in addition to the inherent ripples coming from sudden change in electric potential.



(a) Focusing Magnet



(b) Defocusing Magnet



(c) Choke

Figure 10 | One focusing magnet, one defocusing magnet, and one choke constitute each magnet cell of the equivalent-circuit model.

Such EMI problems thereby worsen and give rise to larger current fluctuations, or common-mode currents, or severe system damage.

5. STOCHASTIC PROCESS FOR MODELLING ELECTRIC-CURRENT RIPPLES

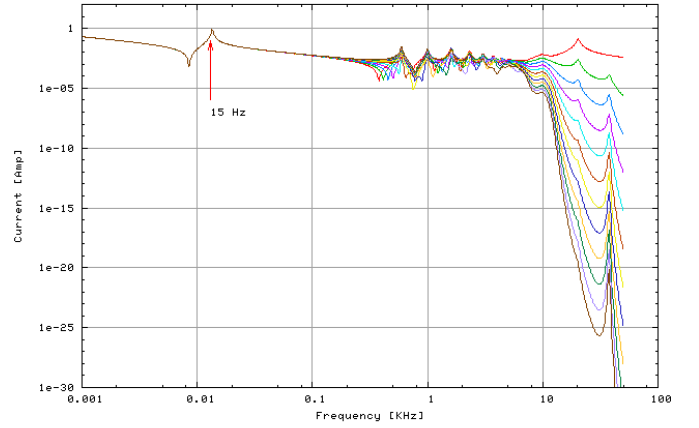


Figure 11 | Currents in frequency domain generated by SPICE simulations; a single power supply drives currents flowing through a string of 12 magnet cells. Progressing from top to bottom, the traces correspond to magnet cell [1] through [12].

Of a variety of stochastic processes¹, the Ornstein-Uhlenbeck process was elected as considered the most proper process for modelling fluctuations in electric currents, based upon our observations and measurements.

5.1. Langevin Equation

Langevin Equation (LE) is the first example of the stochastic differential equations (SDEs)[11, 12]. Paul Langevin devised the equation of motion for a free particle in Brownian motion, according to Newton's second law. It is assumed that a Brownian particle is subject to two forces originating from the surroundings or heat bath: *damping force* \mathbf{F}_d and *fluctuating force* \mathbf{F}_f . To adapt LE to our model, a Langevin-like SDE was formulated by introducing the third term of space-charge force \mathbf{F}_{sc} .

$$\mathbf{F}(\mathbf{v}, t) = \mathbf{F}_d(\mathbf{v}, t) + \mathbf{F}_f(\mathbf{v}, t) + \mathbf{F}_{sc}(\mathbf{v}, t) \quad (2)$$

$$m \frac{d^2 x(t)}{dt^2} = \underbrace{-\mu \frac{dx(t)}{dt}}_{\text{systematic force}} + \underbrace{\mathbf{F}_f(t)}_{\text{stochastic force}} + \underbrace{\mathbf{F}_{sc}}_{\text{space-charge force}} \quad (3)$$

Here, $\mathbf{F}(\mathbf{v}, t)$, m , $x(t)$, and μ represent respectively the total force, particle mass, displacement, and the friction coefficient. The first term $-\mu \dot{x}(t)$ on the right-hand side of Eqn. (3) denotes the viscous drag as a function of time, or dynamic friction.

¹Throughout this Article, we use the following terms interchangeably: *stochastic process*, *stochastic function*, *random process*, *random function*, and *process*.

The second term $F_f(t)$ represents fluctuations emerging from white noise. The form of Eqn. (3) can be transformed into Eqn. (4) of the first order. For modelling physical noise of the Booster's power system, *non-white* noise or *off-white* noise was employed.

$$\frac{dv}{dt} + \alpha v(t) = \mathcal{L}(t), \quad (4)$$

where $\mathcal{L}(t)$ is a stochastic driving force, and α represents μ/m as a damping factor. The following assumptions about the fluctuating part $\mathcal{L}(t)$ are made:

- (1) $\mathcal{L}(t)$ is a function of time only and independent of x .
- (2) zero-mean distribution:

$$\langle \mathcal{L}(t) \rangle = 0 \quad (5)$$

- (3) The variation rate of $\mathcal{L}(t)$ is even higher than the velocity of a Brownian particle $v(t)$. Hence, the autocorrelation function $C_{\mathcal{L}}(t, t')$ is of Dirac- δ function: *i.e.*,

$$C_{\mathcal{L}}(t, t') = \langle \mathcal{L}(t)\mathcal{L}(t') \rangle = A\delta(t - t') \quad (6)$$

The foregoing expressions define the statistical properties of $\mathcal{L}(t)$. For simulated stochastic coloured noise, the LE has a distinctive advantage over the Fokker-Planck Equation (FPE), which poses mathematical complication. The Langevinian method is much easier to understand than the FPE since it is based upon the time evolution of a stochastic variable, whereas the FPE applies to the time evolution of the probability distribution. As such, the Langevinian method has a distinctive advantage of dispensing with the calculation of the diffusion coefficient, thus reducing associated mathematical complications. As a consequence, the data-driven numerical model we constructed is computationally efficient, and far more simplified for studying time-varying stochastic noise of interest.

5.2. Ornstein-Uhlenbeck Process

As in Eqn. (4), the LE for Brownian motion is given as,

$$\dot{\xi}(t) + \omega \xi(t) = \mathcal{L}(t) \quad (7)$$

The LE is associated with δ -correlated Gaussian stochastic forces with statistical properties. This stochastic process $\xi(t)$ is referred to as an O-U process. Note that the noise strength A is not dependent upon the variables ξ . Since the O-U stochastic process inherently represents the velocity of a Brownian particle, it is an appropriate choice of stochastic process for mod-

elling electric noise, or current fluctuations [4]; *i.e.*, a time-derivative of electric charge dQ/dt . Both position $x(t)$ and velocity $v(t)$ describe the Langevinian Brownian motion. However, by utilising the O-U process of the velocity of a Brownian particle, the LE can be reduced to a first-order, first-degree linear stochastic differential equation that is derived from Newton's second law. As a result, the LE becomes straightforward first-order, first-degree SDE to find solutions.

The O-U process is associated with an exponentially-decreasing autocorrelation function $C_{\xi}(t, t')$ [13] and a finite autocorrelation time τ_{ac} [4]².

$$C_{\xi}(t, t') = \langle \xi(t)\xi(t') \rangle = A \exp(-\omega_{ac}|t - t'|), \quad (8)$$

where $\tau_{ac} = \omega_{ac}^{-1}$,

in which $\xi(t)$, ω_{ac} , and A are a stochastic function, an autocorrelation frequency, and a constant for noise strength, respectively. Further, the O-U process is associated with the following probability density function:

$$W_1(\xi, t) = \frac{1}{\sqrt{\pi A/\omega_{ac}}} \cdot \exp\left(-\frac{1}{2} \frac{\xi^2}{A/2\omega_{ac}}\right) \quad (9)$$

According to Doob's theorem [14], the O-U process is the only stochastic process having all of the following properties: (1) stationary process, (2) Gaussian process, and (3) Markovian process.

$$\langle \xi(t_1 + \alpha)\xi(t_2 + \alpha) \cdots \xi(t_n + \alpha) \rangle = \langle \xi(t_1)\xi(t_2) \cdots \xi(t_n) \rangle \quad (10)$$

where $\xi(t)$ is a stochastic function and $\langle \dots \rangle$ is a statistical average. The form of Eqn. (10) implies the followings:

- (1) Since the underlying mechanisms causing the fluctuations do not change with time, the stochastic properties of a stationary process are conserved.
- (2) The important parameter in the O-U process is *relative time* and not the absolute time.

$$\langle \xi(t_1 - \alpha)\xi(t_1) \rangle = \langle \xi(t_1)\xi(t_1 + \alpha) \rangle \quad (11)$$

Therefore, the autocorrelation function $C_{\xi}(t, t')$ for a stationary process is a function of $|t - t'|$ only.

²The autocorrelation function $C(t, t')$ determines the property of a stochastic process of interest.

- (3) Its ensemble average equates to its time average, thus leading to the ergodic property.

5.3. Markov Process

Markov processes involve the use of *conditional probability*.

$$W_2(\xi_1, \xi_2, t) = W_1(\xi_1)p_2(\xi_1 | \xi_2, t) \quad (12)$$

The Markov process is therefore defined thus [5]:

$$p_n(\xi_1 t_1, \xi_2 t_2, \dots, \xi_{n-1} t_{n-1} | \xi_n t_n) = p_2(\xi_{n-1} t_{n-1} | \xi_n t_n) \quad (13)$$

The form of Eqn. (13) implies that all the p_n for $n > 2$ can be derived, when only p_2 is known. Put it simply,

Only the present condition determines the future condition.

In order to avoid unnecessary mathematical complexity in building a stochastic noise model, we exploited the Markovian property. This is another reason why, of all the stochastic processes, the O-U process is the most convenient choice for modelling the power-supply current ripples.

6. GENERATING FREQUENCY-DEPENDENT STOCHASTIC NOISE

This section concerns how to devise and embed the numerical algorithm for generating time- and frequency-dependent stochastic noise in the new noise module.

6.1. Stochastic Properties

Langevin equation governs the O-U process. For basing the model of current ripples on the O-U process, Langevin-like equation has been formulated and solved. One can extract more statistical properties of the O-U process beyond the posterior properties by solving the convenient first-degree, first-order linear Langevin-like equation: Eqns. (5), (6), and (9). Let us first consider the first-order SDE in the form of LE.

$$\dot{\xi}(t) = f(\xi) + \eta(t) \quad (14)$$

Here $\eta(t)$ is non-white Gaussian noise with its autocorrelation function C_η :

$$C_\eta(t, t') = \langle \eta(t)\eta(t') \rangle = \frac{\mathcal{A}}{2\omega_{ac}} \exp(-\omega_{ac}|t - t'|) \quad (15)$$

LE governs non-white noise $\eta(t)$ with a white-noise driving force of $\mathcal{L}(t)$:

$$\dot{\eta}(t) + \omega_{ac}\eta(t) = \mathcal{L}(t) \quad (16)$$

The autocorrelation function $C_\mathcal{L}$ is δ -correlated with a strength \mathcal{A} :

$$C_\mathcal{L}(t, t') = \langle \mathcal{L}(t)\mathcal{L}(t') \rangle = \mathcal{A}\delta(t - t') \quad (17)$$

Ornstein and Uhlenbeck [4], Doob [14], and van Kampen [5] used the integration method to determine the statistical properties of non-white noise, or coloured noise from LE. We, on the other hand, solved LE as a first-order differential equation. Hence, the following solution to LE was worked out:

$$\eta(t) = \eta(0) \exp(-\omega_{ac} t) + \int_0^t ds \cdot \exp(-\omega_{ac}(t-s)) \mathcal{L}(s) \quad (18)$$

The stochastic process at the next time step $t + \Delta t$ can be found from Eqn. (18):

$$\begin{aligned} \eta(t + \Delta t) &= \eta(0) \exp(-\omega_{ac}(t + \Delta t)) + \int_0^{t + \Delta t} ds \exp(-\omega_{ac}(t + \Delta t - s)) \mathcal{L}(s) \\ &= \eta(t) \exp(-\omega_{ac}\Delta t) + \underbrace{\int_t^{t + \Delta t} ds \exp(-\omega_{ac}(t + \Delta t - s)) \mathcal{L}(s)}_{H(t, t + \Delta t)} \end{aligned} \quad (19)$$

By transforming the variables of integration, one can arrive at

$$\begin{aligned} H(0, \Delta t) &= \int_0^{\Delta t} d\tilde{s} \cdot \exp(-\omega_{ac}(\Delta t - \tilde{s})) \mathcal{L}(\tilde{s} + t) \\ &= \exp(-\omega_{ac}\Delta t) \int_0^{\Delta t} d\tilde{s} \cdot \exp(\omega_{ac}\tilde{s}) \mathcal{L}(\tilde{s} + t) \end{aligned} \quad (20)$$

Further, one can derive the following by squaring Eqn. (20):

$$\begin{aligned} \{H(0, \Delta t)\}^2 &= \exp(-2\omega_{ac}\Delta t) \int_0^{\Delta t} \int_0^{\Delta t} d\tilde{s} d\tilde{s}' \exp(\omega_{ac}(\tilde{s} + \tilde{s}')) \mathcal{L}(\tilde{s} + t) \mathcal{L}(\tilde{s}' + t) \end{aligned} \quad (21)$$

The statistical properties of a stochastic variable can be studied by calculating various moments. Accordingly, the first and the second central moments were calculated by averaging Eqns. (20) and (21) over an ensemble of particles. For zero-mean Gaussian, the 1st moment vanishes: $\langle H(0, \Delta t) \rangle = 0$

Cognisant of the fact that the O-U process is a stationary process, the 2nd moments boil down to the following:

$$\begin{aligned} & \langle \{H(0, \Delta t)\}^2 \rangle \\ &= \exp(-2\omega_{ac}\Delta t) \int_0^{\Delta t} \int_0^{\Delta t} d\tilde{s} d\tilde{s}' \exp(\omega_{ac}(\tilde{s} + \tilde{s}')) \langle \mathcal{L}(\tilde{s}) \mathcal{L}(\tilde{s}') \rangle \\ &= \mathcal{A} \exp(-2\omega_{ac}\Delta t) \int_0^{\Delta t} d\tilde{s} \exp(2\omega_{ac}\tilde{s}) \\ &= \frac{\mathcal{A}}{2\omega_{ac}} \{1 - \exp(-2\omega_{ac}\Delta t)\} \end{aligned} \quad (22)$$

The second moments of $H(0, \Delta t)$ can be expanded in a closed form as in Eqn. (23).

$$\begin{aligned} \langle \{H(0, \Delta t)\}^2 \rangle &= \frac{\mathcal{A}}{2\omega_{ac}} \{1 - \exp(-2\omega_{ac}\Delta t)\} \\ &= \mathcal{A} \Delta t \left[1 - R_t + \frac{2}{3} R_t^2 - \frac{1}{3} R_t^3 + \dots \right], \end{aligned} \quad (23)$$

with R_t being $\omega_{ac}\Delta t$. What determines the $\langle H^2 \rangle$ is $\omega_{ac}\Delta t$ that is time step Δt in units of autocorrelation time τ_{ac} , not autocorrelation time, or time step by itself. This noise module was inherently designed to generate the O-U stochastic noise $\eta(t)$ to be applied to macroparticles in the form of magnetic-field perturbations: *autocorrelation time* τ_{ac} , *time step* Δt , and *noise strength* \mathcal{A} .

6.2. Box-Muller-Like Transformation

The Box-Muller transformation [16, 17] is intrinsically for generating independent Gaussian white noise—which is a limiting case of physical noise—from independent uniform random deviates. In order to generate exponentially-driven Gaussian stochastic noise, an exponential factor $\exp(-\omega\Delta t)$ is first multiplied by the stochastic noise $\eta(t)$ at present time t . Then, an r.m.s. value of $H(0, \Delta t)$ is added to compute the noise at the next time step $t + \Delta t$.

$$\begin{aligned} \eta(t + \Delta t) &= \exp(-\omega\Delta t) \eta(t) + C_W \sqrt{\langle H(t, t + \Delta t)^2 \rangle} \\ &= \exp(-\omega\Delta t) \eta(t) + C_W \sqrt{\langle H(0, \Delta t)^2 \rangle}, \end{aligned} \quad (24)$$

where C_W denotes random deviates from a rectangular distribution (or white noise). What Eqn. (24) implies is that generating $\eta(t + \Delta t)$ requires one to know $\eta(t)$ only. This takes advantage of the powerful *Markov property* belonging to the O-U process in numerical calculations. Upon providing with stochastic parameters, the variant of the Box-Muller transformation is capable of generating a wide spectrum of stochastic noise in both time and frequency domains: *coloured noise*, *non-white noise*, *off-white noise*, *white noise*, etc. Graphed in Supplementary Figure 6 are the sample paths of noise with differing stochastic parameters. The time step is fixed at one revolution period of circulating proton beams at the Booster's injection energy. As can be seen from Supplementary Figure 6, the autocorrelation time governs the pattern of sample path. It is, therefore, evident that the pattern of all sample paths are *aperiodic*.

6.3. Application of Stochastic Noise to Macroparticles

This noise model takes in measurements of current ripples translating linearly into magnetic-field undulations, as in Eqn. (25).

$$\tilde{\mathbf{K}}_{imag} = \mathbf{K}_{imag} + |\Delta \mathbf{K}_{imag}| = \mathbf{K}_{imag} \cdot \left(1 + |\Delta \mathbf{K}_{imag}| / |\mathbf{K}_{imag}|\right), \quad (25)$$

where the subscript *imag* denotes magnet index for differentiating between individual main dipole magnets. In order to distinguish field fluctuations at each type of magnet (focusing, or defocusing), \mathbf{K}_{imag} is factored out, and the amount of field variation $\Delta \mathbf{K}_{imag}$ is normalized by \mathbf{K}_{imag} as a perturbation term.

7. BEAM TRACKING AND DIAGNOSIS

7.1. Simulation Parameters

A comprehensive set of machine parameters for the Booster ring at an injection energy is summed up in Table 2. In addition, key parameters of ORBIT-FERMI including space-charge calculations are abstracted in Table 3. Prior to tracking, injecting into the Booster ring a round beam with axisymmetry and uniform charge distributions, ensures that one can solely investigate the noise-induced phenomena under the full space-charge conditions alone.

7.2. Moments

We present how various measures of beam diagnosis are defined and computed in this stochastic noise model. Moments

Table 2 | Machine parameters for Fermilab's Booster at an injection energy.

ring radius ($\langle R \rangle$)	75.47 (m)
ring circumference	474.2 (m)
injection kinetic energy	400 (MeV)
synchronous energy (E_s)	1.328 (GeV)
β (Lorentz factor)	0.7131
γ (Lorentz factor)	1.426
revolution period (T_0)	2.2 (μ s)
number of injection turns	11
injection period	24.2 (μ s)
cycle time	66.7 (ms)
γ_{tr} (transition gamma)	5.4696
α_1 (momentum compaction factor)	0.0172
phase-slip factor ($ \eta $)	0.458
$\epsilon_{tr,95,n}$ (95 %, normalized)	12.0 (π -mm-mrad)
RF range	38.18 \sim 52.83 (MHz)
ν_{x0}/ν_{y0} (bare tunes)	6.7 / 6.8
betatron frequency ($f_{\beta,x}, f_{\beta,y}$)	318.2 / 363.6 (kHz)
Q_s (synchrotron tune)	1.147×10^{-3}
Ω_s (synchrotron frequency)	3.28 (kHz)
T_s (synchrotron period)	305 (μ s)
σ_z (r.m.s. bunch length)	1.0 (m)
β_z (longitudinal beta function)	3.0×10^4 (m)
ϵ_L (longitudinal emittance)	0.25 (eV-s)
batch intensity	5.04×10^{12}
average beam current (at injection)	420 (mA)
effective beam radius	0.0325 (m)
bunching factor (B_f)	~ 0.4
Δv (space-charge tune shifts)	- 0.4
$\Delta P/P_0 _{max}$	± 0.15 %
σ_δ	3.0×10^{-4}
$\beta_{x,max} / \beta_{y,max}$	33.7 / 20.5 (m)
$D_{x,max} / D_{y,max}$	3.2 / 0.0 (m)
cell type	FOFDOOD
cell length	20.62 (m)
gradient magnets / cell	4
total gradient magnets	96
$V_{rf,inj}$ (RF voltage at injection)	205.0 (kV/Turn)
phase advance / cell	96 (deg)
ρ_D (defocusing bending radius)	48.034100 (m)
ρ_F (focusing bending radius)	40.847086 (m)

Table 3 | Key simulation parameters (ORBIT-FERMI) for the Booster. LSC and TSC stand respectively for longitudinal and transverse space charge.

no. of injection turns	11
no. of max. macroparticles	330,000
harmonic number	84
beam kinetic energy	400.0 (MeV)
beam intensity (per RF bucket)	6.0×10^{10}
transverse beam distribution	bi-Gaussian
ring circumference	474.2 (m)
$\beta_{x,inj} \beta_{y,inj}$	6.274 / 19.312 (m)
$\alpha_{x,inj} \alpha_{y,inj}$	-0.122 / 0.024
$D_{x,0} D_{y,0}$	2.581 / 0.0 (m)
$x_{0,inj} y_{0,inj}$	0.0 / 0.0 (mm)
E_{offset}	0.0 (GeV)
$\Delta E/E_{kinetic}$	5.1×10^{-4}
$\epsilon_{x,rms,inj} \epsilon_{y,rms,inj}$	1.76 / 1.76 (π -mm-mrad)
V_{rf} (RF voltage)	205.0 (kV/Turn)
R_{wall}/R_{beam} (for geometric factor)	2.0
LSC bin no.	32
TSC bin no.	64 x 64
smoothing parameter	$\sim 10^{-6}$
min. no. of particles/LSC bin	16
min. no. of particles/TSC bin	128
no. of total tracking turns	1,000

are defined to characterise probability distributions of a beam, or macroparticles. Since it is essential to consider beam motions, the ORBIT-FERMI simulations employ central moments in transverse planes ($\langle x \rangle$ and $\langle y \rangle$) at the onset:

$$\begin{cases} \Delta x_r = x_r - \langle x_r \rangle \\ \Delta y_r = y_r - \langle y_r \rangle, \end{cases} \quad (26)$$

where $x_r(z)$ and $y_r(z)$ denote real-space coordinates. Because of vanishing central-moment calculations, beam centroids themselves ($\langle x \rangle$ and $\langle y \rangle$) are used for the 1st-moment calculations. It is assumed that the density profiles of an actual beam in transverse planes are *bi-Gaussian*. Upon injection of a herd of macroparticles of bi-Gaussian distribution, one can compute the 2nd-moments for calculating r.m.s. beam sizes (σ_x, σ_y):

$$1^{st} \text{ moments} \begin{cases} \langle x_r \rangle \\ \langle y_r \rangle \end{cases} \quad (27)$$

$$2^{nd} \text{ moments} \begin{cases} \sigma_x^2 = \langle (\Delta x_r)^2 \rangle \\ \sigma_y^2 = \langle (\Delta y_r)^2 \rangle \end{cases} \quad (28)$$

The r.m.s. beam sizes are important for space-charge study. Starting with the bi-Gaussian charge distribution $\rho(r)$, we can derive transverse space-charge force $F_{sc}(r)$, using Gauss' and Ampère's laws. The transverse r.m.s. beam sizes σ_r determine

the range of linear transverse space-charge forces $F_{sc}(r)$ (Eqn. (29)): and $M_{2,y}$ were constructed:

$$\begin{cases} \rho(r) = \frac{Ne}{2\pi\sigma_r^2} \exp\left(-\frac{r^2}{2\sigma_r^2}\right) \\ \vec{F}_{sc}(r) = \frac{Ne^2}{2\pi\epsilon_0\gamma^2 r L_b} \left(1 - \exp\left(-\frac{r^2}{2\sigma_r^2}\right)\right) \hat{r} \\ r = \sqrt{x^2 + y^2} \end{cases} \quad (29)$$

where N , e , ϵ_0 , σ_r , γ , r , and L_b denote the number of particles per length, unit charge, permittivity of vacuum, r.m.s. beam size, Lorentz factor, radial distance, and bunch length, respectively. The transverse space-charge forces grow linearly with transverse displacements (x , or y), and scale off ($\propto 1/r$) with displacements larger than $2\sigma_r$. According to the evolution of the 2nd-moment calculations, the r.m.s. beam sizes grow steadily without cease in the presence of the full space charge forces and power-supply ripples. To understand the time evolution of r.m.s. beam sizes, or r.m.s. beam widths in transverse planes, the 2nd moments in real physical space are computed.

$$\begin{cases} x_r(z) = x_\beta(z) + D_x(z) \cdot \frac{\Delta p}{p_0} \\ y_r(z) = y_\beta(z) \end{cases} \quad (30)$$

In Eqn. (30), $x_\beta(z)$ and $y_\beta(z)$ denote betatron coordinates, and $D_{x0}(z)$ and p_0 respectively denote injection horizontal dispersion and design momentum. In a similar fashion, divergence angles are computed:

$$\begin{cases} x'_r(z) = x'_\beta(z) + D'_x(z) \cdot \frac{\Delta p}{p_0} \\ y'_r(z) = y'_\beta(z), \end{cases} \quad (31)$$

where $D'_x(z)$ denotes the slope of horizontal dispersion.

7.3. Emittances

Since the ORBIT-FERMI simulations employ the 2nd-order central moments for calculating r.m.s. emittances, a few measures were defined thus:

$$\begin{cases} \Delta p_x \equiv p_x - \langle p_x \rangle \\ \Delta p_y \equiv p_y - \langle p_y \rangle \end{cases} \quad (32)$$

For computing the 2nd-order central moments of each individual coordinate in the 6-dimensional space, column matrices $M_{2,x}$

$$M_{2,x} = \begin{bmatrix} \Delta x_\beta \\ \Delta x'_\beta \end{bmatrix} \quad M_{2,y} = \begin{bmatrix} \Delta y_\beta \\ \Delta y'_\beta \end{bmatrix} \quad (33)$$

With the column matrices M_2 above, 2×2 Σ -matrices were defined in subspaces of trace space: (x_β, x'_β) and (y_β, y'_β) . In each of Σ -matrices, the off-diagonal elements are associated with the correlation between positions and angles, or energy and RF phase [21].

$$\begin{aligned} \Sigma(x_\beta, x'_\beta) &\equiv \langle M_{2,x_\beta} M_{2,x_\beta}^T \rangle \\ &= \begin{bmatrix} \langle (\Delta x_\beta)^2 \rangle & \langle \Delta x_\beta \Delta x'_\beta \rangle \\ \langle \Delta x'_\beta \Delta x_\beta \rangle & \langle (\Delta x'_\beta)^2 \rangle \end{bmatrix} \end{aligned} \quad (34)$$

in which M^T denotes a transpose matrix of M . Using the 2×2 Σ -matrix, an *unnormalized r.m.s. emittance* can be defined as follows:

$$\begin{aligned} \epsilon_{x,rms} &= \sqrt{\det \Sigma(x_\beta, x'_\beta)} \\ &= \sqrt{\langle (\Delta x_\beta)^2 \rangle \langle (\Delta x'_\beta)^2 \rangle - \underbrace{\langle \Delta x_\beta \Delta x'_\beta \rangle^2}_{\text{correlation term}}} \end{aligned} \quad (35)$$

Transverse r.m.s. emittances are defined in $(x_\beta, p_x/p_0)$ and $(y_\beta, p_y/p_0)$ phase spaces, following the MAD [22] convention:

$$\Sigma(x_\beta, p_x) = \begin{bmatrix} \langle (\Delta x_\beta)^2 \rangle & \langle \Delta x_\beta \Delta p_x \rangle \\ \langle \Delta p_x \Delta x_\beta \rangle & \langle (\Delta p_x)^2 \rangle \end{bmatrix} \quad (36)$$

$$\begin{aligned} \epsilon_{x,rms} &= \frac{1}{p_0} \sqrt{\det \Sigma(x_\beta, p_x)} \\ &= \frac{1}{\gamma\beta m_0 c} \sqrt{\langle (\Delta x_\beta)^2 \rangle \langle (\Delta p_x)^2 \rangle - \langle \Delta x_\beta \Delta p_x \rangle^2}, \end{aligned} \quad (37)$$

in which the transverse momenta (p_x and p_y) are normalized by the design momentum (p_0). The Eqns. (33) through (37) apply likewise to vertical and longitudinal planes.

$$\begin{cases} \epsilon_{x,n,rms} &= (\beta\gamma)\epsilon_{x,rms} \\ &= (\beta\gamma) \sqrt{\langle (\Delta x_\beta)^2 \rangle \cdot \langle (\Delta x'_\beta)^2 \rangle - \langle \Delta x_\beta \Delta x'_\beta \rangle^2} \\ &= \frac{1}{m_0 c} \sqrt{\langle (\Delta x_\beta)^2 \rangle \langle (\Delta p_x)^2 \rangle - \langle \Delta x_\beta \Delta p_x \rangle^2} \\ \epsilon_{y,n,rms} &= (\beta\gamma)\epsilon_{y,rms} \\ &= (\beta\gamma) \sqrt{\langle (\Delta y_\beta)^2 \rangle \langle (\Delta y'_\beta)^2 \rangle - \langle \Delta y_\beta \Delta y'_\beta \rangle^2} \\ &= \frac{1}{m_0 c} \sqrt{\langle (\Delta y)^2 \rangle \langle (\Delta p_y)^2 \rangle - \langle \Delta y \Delta p_y \rangle^2} \end{cases} \quad (38)$$

8. IMPACT OF ELECTRIC-CURRENT FLUCTUATIONS UNDER SPACE-CHARGE FORCES

Four random-noise nodes, provided with characteristic noise parameters, are inserted into the lattice of the Booster ring. Macroparticles representing proton beams are tracked over 1,000 turns in the presence of full space charge³. As shown in Figure 12, the time evolution of transverse r.m.s. emittances with the space-charge forces alone (blue) and with the O-U noise coupled to the full space-charge forces (red). The beam intensity per bucket is 6.0×10^{10} protons per bucket (ppb), and one batch intensity is 5.0×10^{12} protons. To estimate the emittance growth rate prior to accelerating beams, the relative emittance growths ($\Delta\epsilon/\epsilon_0$) are calculated, starting from the final injection turn (the 11th turn) through 1,000 turns—this corresponds to the first 2.2 ms out of one revolution period of 66.7 ms (15 Hz). The relative emittance growth ($\Delta\epsilon/\epsilon_0$) is about 7.5 % in the horizontal plane, and 9.3 % in the vertical plane. Simulated and tracked are a total of 330,000 macroparticles amassed by repeatedly injecting 30,000 macroparticles per injection turn. Upon inclusion of the O-U noise representing the ripples under space charge, the beam-degrading process is set in development, thereby forming more noticeable halos. As a cross-check with the calculations of r.m.s. emittances, average actions (J_x and J_y) were computed at each tracking turn under the same conditions. For clear comparison, the r.m.s. emittances and average actions are overlaid in Figure 13. Calculating both r.m.s. emittances and actions manifests in such a good agreement that beam-degrading process is substantially enhanced due to *synergistic mechanism* between fluctuational power-supply currents and space-charge forces. The time evolution of r.m.s. beam sizes in both transverse planes with space charge alone and with the ripples and space charge are illustrated in Figure 14. With the O-U noise added, the 2nd moments of the beams (beam size squared) grow faster than in the case for space charge alone as beams circulate. If we lower under the same conditions the Booster's batch intensity by an order of one magnitude (5×10^{11}) than the operational batch intensity, emittance growths induced by the ripples and space-charge effects are indistinguishable from those by noise alone, without space-charge effects (Figure 15). This is a clear signature implying that only when the space-charge effects are substan-

tial, the power-supply ripples exert considerable influence on the Booster's beams.

8.1. Couplings

On top of the primary calculations—r.m.s. emittances and average actions— we looked into the transverse couplings as well. Computing the 2nd-order cross moment $\langle xy \rangle$ for each case is presented in Figure 18. A marginal amount of couplings are introduced when the full space-charge effects are present with no power-supply noise (Figure 18 (b)). When the noise is included alone in the absence of the space charge, couplings are somewhat noticeable (Figure 18 (c)). When the power-supply noise and the full space-charge effects are included, the transverse couplings are increasingly noticeable. It is thus concluded that the power-supply noise impacting upon a proton beam is dependent upon the strengths of the space-charge defocusing forces in the Booster. What Figure 16 illustrates is the percentage of macroparticles displaced outside of a given average action when the power-supply noise coexists with the full self-fields. The blue markers indicate the fraction of excluded macroparticles at a given emittance at the first tracking turn and the red markers after 1,000 turns. Compared in Figure 17 are the distributions of transverse single-particle actions (J_x and J_y) at the outset of injection and at the 1,000th turn. It becomes evident that noise-induced beam degradation is escalated as time elapses.

8.2. Coupling Magnitudes

In an ideal system, the normalized r.m.s. emittance remains invariant. However, nonlinear space-charge forces and couplings can induce such processes of degrading beam properties. The increases of the normalized r.m.s. emittances indicate that nonlinear space-charge effects and couplings induced by different types of machine imperfections are existent in the Booster. One of the great advantages of performing accelerator simulations by tracking huge herds of macroparticles is that one can isolate a system condition to pin down a specific cause of growing emittances under investigation. Therefore, we looked into the transverse couplings by implementing in ORBIT-FERMI new parallel calculations of 4-dimensional transverse emittances (ϵ_{xy}^4) and coupling magnitudes. One can also calculate a squared 2-dimensional r.m.s. emittance on the horizontal plane from the determinant of 2×2 Σ -matrix of beam distributions (Eqn. (36))

³In the present context, the full space charge is referred to as both transverse and longitudinal space charge, or 3-D space charge.

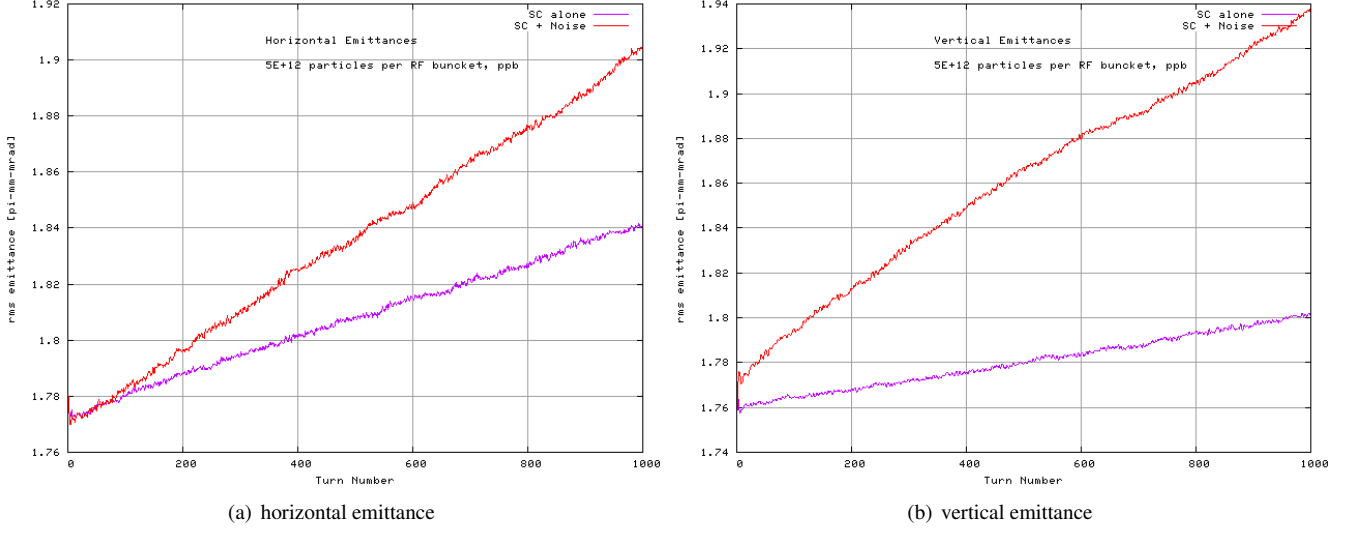


Figure 12 | Growing transverse r.m.s. emittances, starting from the outset of injection through 1,000 tracking turns.

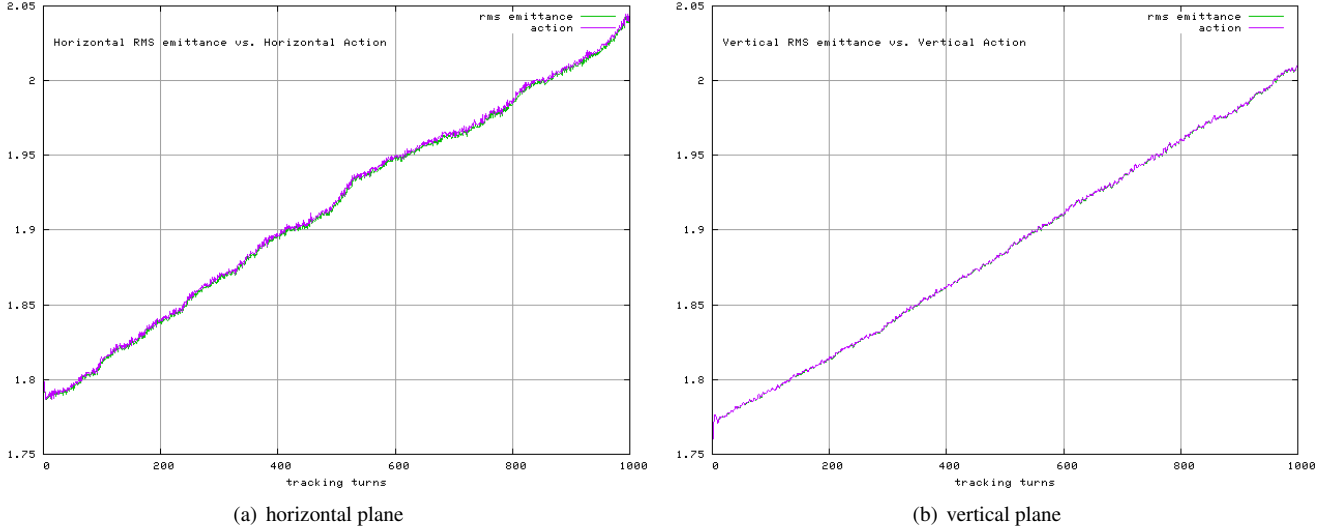


Figure 13 | Time evolution of r.m.s. emittances in comparison with actions: (a) horizontal r.m.s. emittance vs. horizontal action; (b) vertical r.m.s. emittance vs. vertical action.

and likewise for the counterpart on the vertical plane.

$$\epsilon_{x,rms}^2 = \det \begin{vmatrix} \langle (\Delta x_\beta)^2 \rangle & \langle \Delta x_\beta \Delta p_x \rangle \\ \langle \Delta p_x \Delta x_\beta \rangle & \langle (\Delta p_x)^2 \rangle \end{vmatrix} \quad (39)$$

For computing 4-dimensional r.m.s. emittances and couplings, 4-component column matrices ($M_{4,xy}$, $M_{4,yz}$, and $M_{4,xz}$) are defined on the two planes as described in Eqn. (40). By means of generating 4×4 Σ -matrices with the column matrices as in Eqn. (41), one can calculate the determinant of each 4×4 matrix

as in Eqns. (42) through (43) that follow:

$$M_{4,xy} = \begin{bmatrix} \Delta x_\beta \\ \Delta p_x \\ \Delta y_\beta \\ \Delta p_y \end{bmatrix} \quad M_{4,xz} = \begin{bmatrix} \Delta x_\beta \\ \Delta p_x \\ \delta \tilde{E} \\ \Delta \phi \end{bmatrix} \quad M_{4,yz} = \begin{bmatrix} \Delta y_\beta \\ \Delta p_y \\ \delta \tilde{E} \\ \Delta \phi \end{bmatrix} \quad (40)$$

$$\begin{cases} \Sigma_{xy} = \Sigma(x_\beta, x'_\beta, y_\beta, y'_\beta) = \langle M_{xy} M_{xy}^T \rangle \\ \Sigma_{xz} = \Sigma(x_\beta, x'_\beta, \delta \tilde{E}, \phi) = \langle M_{xz} M_{xz}^T \rangle \\ \Sigma_{yz} = \Sigma(y_\beta, y'_\beta, \delta \tilde{E}, \phi) = \langle M_{yz} M_{yz}^T \rangle, \end{cases} \quad (41)$$

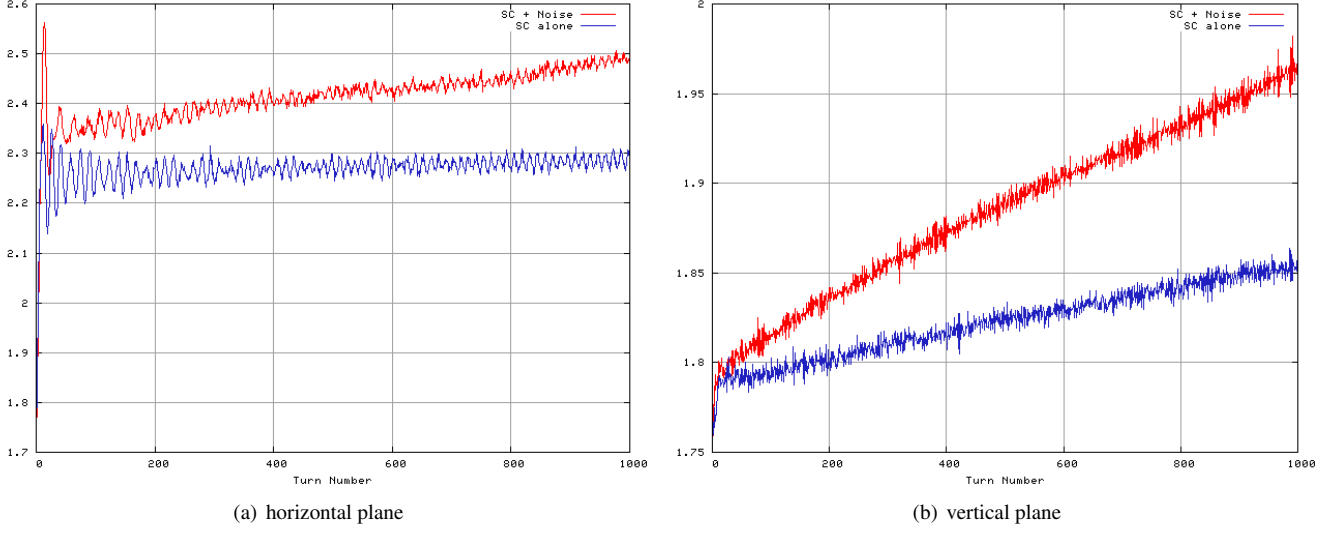


Figure 14 | Time evolution of the 2nd moments in transverse planes; the full space-charge forces alone (blue) and stochastic noise and the full space-charge forces combined (red).

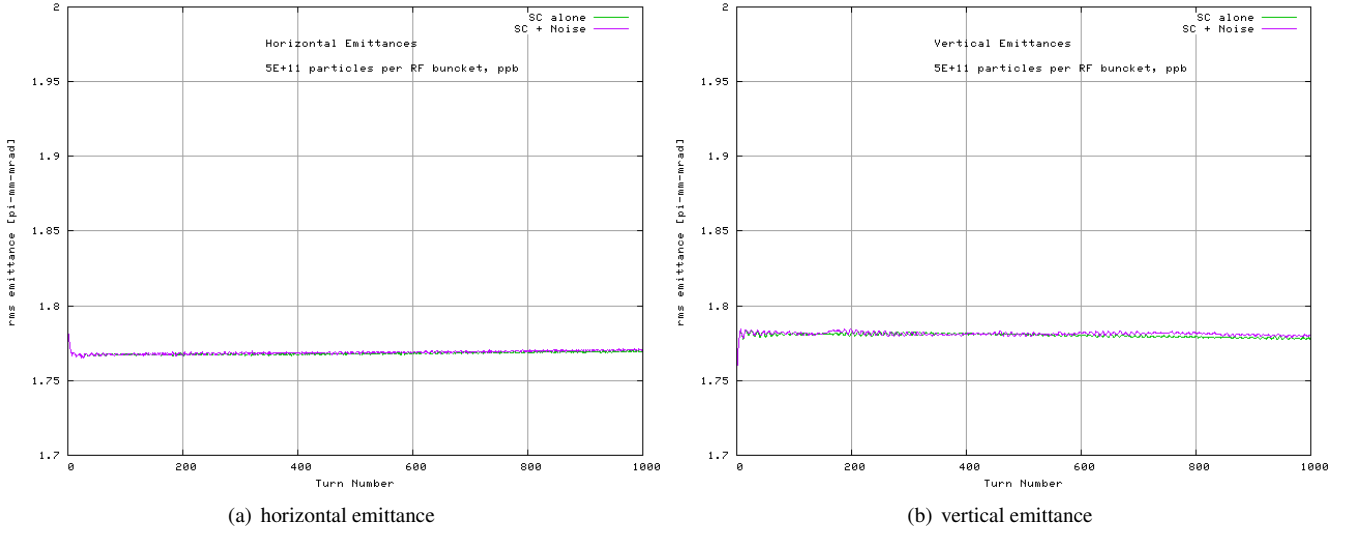


Figure 15 | Growing transverse emittances; the stochastic noise and space-charge effects in red and the space-charge effects alone in blue. The simulated beam intensity is 6×10^9 protons per RF bucket (ppb), and 5×10^{11} protons in total.

in which M^T denotes a transpose matrix of M .

In the same fashion, 4-dimensional emittances and couplings are computed on x - z and y - z planes as well.

$$\epsilon_{xz}^4 = \det \begin{vmatrix} \langle (\Delta x_\beta)^2 \rangle & \langle \Delta x_\beta \Delta p_x \rangle & \langle \Delta x_\beta \delta \tilde{E} \rangle & \langle \Delta x_\beta \Delta \phi \rangle \\ \langle \Delta p_x \Delta x_\beta \rangle & \langle (\Delta p_x)^2 \rangle & \langle \Delta p_x \delta \tilde{E} \rangle & \langle \Delta p_x \Delta \phi \rangle \\ \langle \delta \tilde{E} \Delta x_\beta \rangle & \langle \delta \tilde{E} \Delta p_x \rangle & \langle (\delta \tilde{E})^2 \rangle & \langle \delta \tilde{E} \Delta \phi \rangle \\ \langle \Delta \phi \Delta x_\beta \rangle & \langle \Delta \phi \Delta p_x \rangle & \langle \Delta \phi \delta \tilde{E} \rangle & \langle (\Delta \phi)^2 \rangle \end{vmatrix} \quad (43)$$

$$\epsilon_{xy}^4 = \det \begin{vmatrix} \langle (\Delta x_\beta)^2 \rangle & \langle \Delta x_\beta \Delta p_x \rangle & \langle \Delta x_\beta \Delta y_\beta \rangle & \langle \Delta x_\beta \Delta p_y \rangle \\ \langle \Delta p_x \Delta x_\beta \rangle & \langle (\Delta p_x)^2 \rangle & \langle \Delta p_x \Delta y_\beta \rangle & \langle \Delta p_x \Delta p_y \rangle \\ \langle \Delta y_\beta \Delta x_\beta \rangle & \langle \Delta y_\beta \Delta p_x \rangle & \langle (\Delta y_\beta)^2 \rangle & \langle \Delta y_\beta \Delta p_y \rangle \\ \langle \Delta p_y \Delta x_\beta \rangle & \langle \Delta p_y \Delta p_x \rangle & \langle \Delta p_y \Delta y_\beta \rangle & \langle (\Delta p_y)^2 \rangle \end{vmatrix} \quad (42)$$

$$\epsilon_{yz}^4 = \det \begin{vmatrix} \langle (\Delta y_\beta)^2 \rangle & \langle \Delta y_\beta \Delta p_y \rangle & \langle \Delta y_\beta \delta \tilde{E} \rangle & \langle \Delta y_\beta \Delta \phi \rangle \\ \langle \Delta p_y \Delta y_\beta \rangle & \langle (\Delta p_y)^2 \rangle & \langle \Delta p_y \delta \tilde{E} \rangle & \langle \Delta p_y \Delta \phi \rangle \\ \langle \delta \tilde{E} \Delta y_\beta \rangle & \langle \delta \tilde{E} \Delta p_y \rangle & \langle (\delta \tilde{E})^2 \rangle & \langle \delta \tilde{E} \Delta \phi \rangle \\ \langle \Delta \phi \Delta y_\beta \rangle & \langle \Delta \phi \Delta p_y \rangle & \langle \Delta \phi \delta \tilde{E} \rangle & \langle (\Delta \phi)^2 \rangle \end{vmatrix} \quad (44)$$

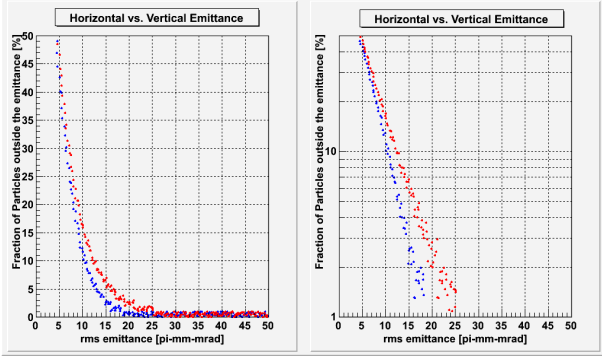


Figure 16 | Fractional exclusion of macroparticles at a given average action. The blue indicates fractional rates at the 1st tracking turn and the red indicates at the 1,000th turns. The vertical axis on the left plot is on a linear scale, and the right plot is on a log scale.

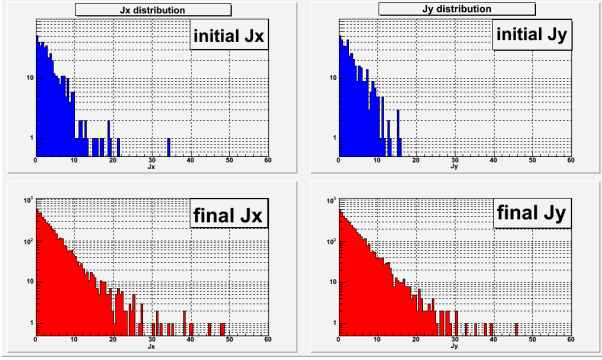


Figure 17 | The distribution of actions (J_x and J_y) at the 1st turn and at the 1,000th tracking turns. The O-U noise and 3-D space-charge forces are included. Action distributions at the first turn is indicated in blue, and action distributions at the 1,000th turns in red.

Hence, the coupling magnitudes between x - y , y - z , and x - z are calculated thus:

$$\begin{aligned}
 \Delta \epsilon_{xy}^4 &= \left| \epsilon_{xy}^4 - \epsilon_x^2 \cdot \epsilon_y^2 \right| \\
 &= \left| \underbrace{\sum C_{xy}(\langle \Delta x_\beta \Delta y_\beta \rangle, \langle \Delta x_\beta \Delta p_y \rangle, \langle \Delta y_\beta \Delta p_x \rangle, \langle \Delta p_x \Delta p_y \rangle)}_{23 \text{ terms}} \right| \\
 \Delta \epsilon_{yz}^4 &= \left| \epsilon_{yz}^4 - \epsilon_y^2 \cdot \epsilon_z^2 \right| \\
 &= \left| \underbrace{\sum C_{yz}(\langle \Delta y_\beta \delta \tilde{E} \rangle, \langle \Delta y_\beta \Delta \phi \rangle, \langle \delta \tilde{E} \Delta p_y \rangle, \langle \Delta p_y \Delta \phi \rangle)}_{23 \text{ terms}} \right| \\
 \Delta \epsilon_{xz}^4 &= \left| \epsilon_{xz}^4 - \epsilon_x^2 \cdot \epsilon_z^2 \right| \\
 &= \left| \underbrace{\sum C_{yz}(\langle \Delta x_\beta \delta \tilde{E} \rangle, \langle \Delta x_\beta \Delta \phi \rangle, \langle \delta \tilde{E} \Delta p_x \rangle, \langle \Delta p_x \Delta \phi \rangle)}_{23 \text{ terms}} \right|
 \end{aligned} \tag{45}$$

where $C_{xy}(\dots)$ denotes coupling terms as a function of $\langle \Delta x_\beta \Delta y_\beta \rangle$, $\langle \Delta x_\beta \Delta p_y \rangle$, $\langle \Delta y_\beta \Delta p_x \rangle$, and $\langle \Delta p_x \Delta p_y \rangle$. Thus, $\Delta \epsilon_{xy}^4$ includes all possible combinations of couplings not only between horizontal and vertical positions, but also between positions and divergence angles in transverse planes. Furthermore, the 4-dimensional couplings can be extended to horizontal and longitudinal planes, and to vertical and longitudinal planes. Figure 18 is an illustration of the 2nd-order cross moment of transverse positions ($\langle \Delta x_r \Delta y_r \rangle$) that enables looking into the transverse couplings in the same vertical scale. In the absence of space charge and the power-supply noise, transverse coupling is not observed. In the presence of space charge, the coupling magnitude is slightly increased, but still marginal. However, with the power-supply noise alone without space charge, the coupling is more noticeable and some perturbations appear over 1,000 turns. When the power-supply noise is coupled to the full space-charge effects, the coupling is boosted. In Figure 19, the turn-by-turn calculations of the cross moments are presented in a form of histogram from which statistics are extracted. The distributions marginally spread out as each type of instability (either space charge, or the power-supply noise) is individually included. When the power-supply noise is applied to macroparticles in the presence of space charge, the r.m.s. value is greater than that of the noise alone by about a factor of two. As derived in Eqn. (45), the coupling between horizontal and longitudinal planes escalates without cease, whilst the power-supply noise coupled to space charge impinges on beams. In Figure 20, progressing from bottom to top, each trace line corresponds to the following cases, respectively: (1) with no space charge, nor the power-supply noise, (2) with the power-supply noise alone, (3) with space charge alone, (4) with the power-supply noise co-existing with the 3-D space-charge forces. It is evident in the Figure 20 that transverse coupling is synergistically amplified when the power-supply noise is coupled to the full space-charge forces, when compared to the other cases. From the calculations of the coupling strengths, $\Delta \epsilon_{xy}$ and $\langle \Delta x_r \Delta y_r \rangle$, consistent results were obtained thus: When space-charge forces are coupled with power-supply ripples their impacts on proton beams can be intensified at resonance frequencies.

8.3. Halo Formation

The computation scheme of maximum extent of the coordinates of displaced macroparticles inside a round beam at each tracking turn is implemented in the noise module. Eqn. (46) includes

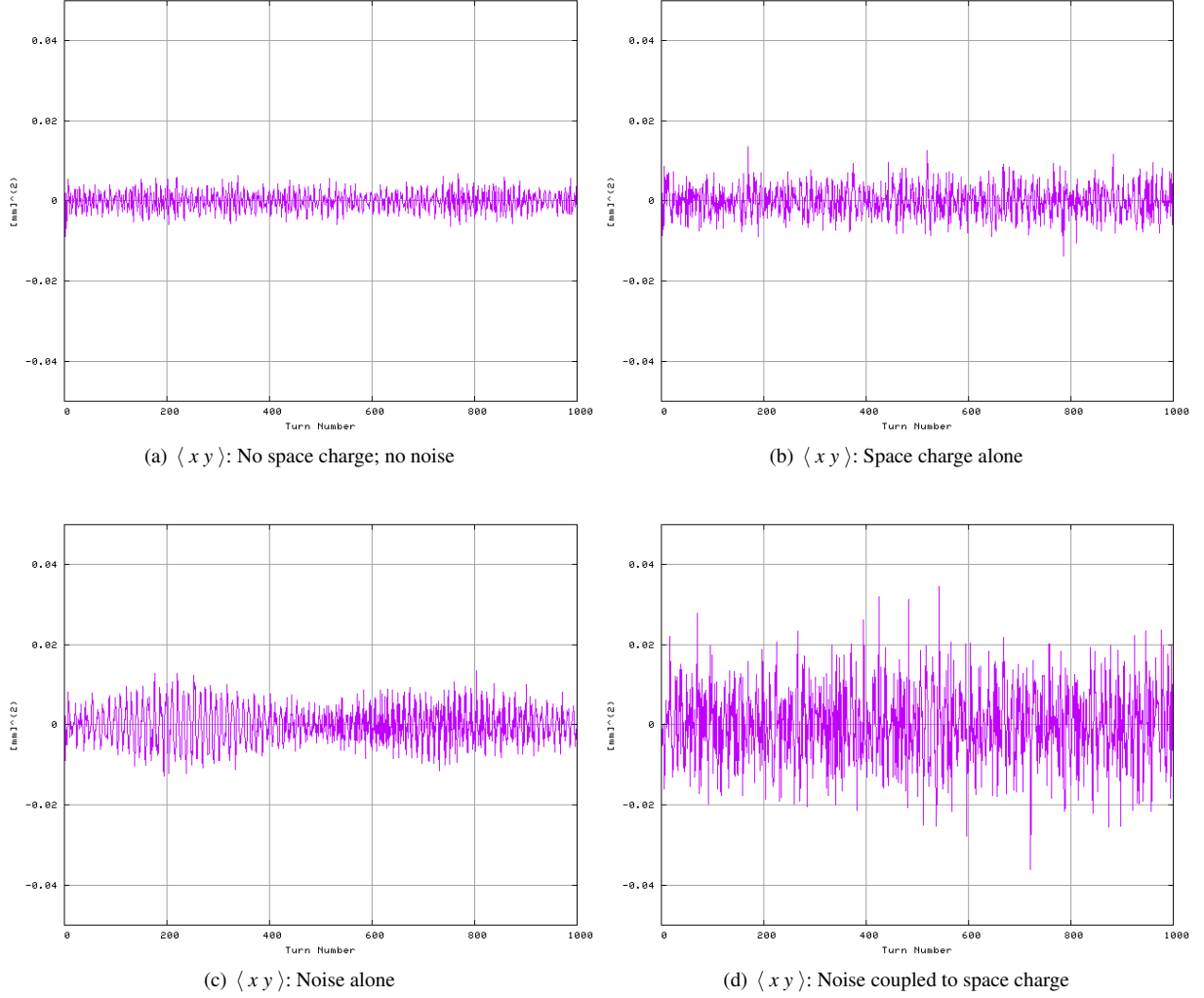


Figure 18 | Transverse couplings in configuration space

only physical coordinates (x and y) of a maximum-displaced macroparticle at the location of a random noise node [2]. It is referred to as the *halo magnitude* $R_{H,2}$:

$$R_{H,2} = \sqrt{x^2 + y^2} \Big|_{max} \quad (46)$$

The *halo magnitude* in 4 dimensions $R_{H,4}$, which includes both horizontal and vertical positions and angles of a maximum-displaced particle, is given in Eqn. (47):

$$R_{H,4} = \left(x / \sqrt{\beta_x} \right)^2 + \left(\sqrt{\beta_x} \cdot x' \right)^2 + \left(y / \sqrt{\beta_y} \right)^2 + \left(\sqrt{\beta_y} \cdot y' \right)^2 \Big|_{max}, \quad (47)$$

where β_x and β_y are optics functions at the location of one noise node. Calculating two types of the halo magnitudes ($R_{H,2}$ and $R_{H,4}$) yields consistent results. As Figure 21 illustrates, the evolution of the halo magnitudes is represented in green and

smoothed data is in blue. Due to large oscillatory behaviour of the halo magnitudes, the data points were smoothed. The smoothed curve in Figure 22 shows with clarity a growing pattern of maximum-displaced macroparticles from the physical centre of magnet's aperture.

9. CLOSING REMARKS AND OUTLOOK

Based upon the measured current ripples from the power supplies, the noise model was tuned up in search of stochastic parameters characterising the ripples under study. Leveraging the state-of-the-art technique of parallel computing for enhanced accuracy enabled incorporating and tracking a sufficiently large number of macroparticles with the 3-D space-charge calculations in a practical amount of computing time. It was subsequently discovered that the existence of a substantial amount of offending ripple currents are induced by common-mode voltages arising from the magnet power system. On the other hand,

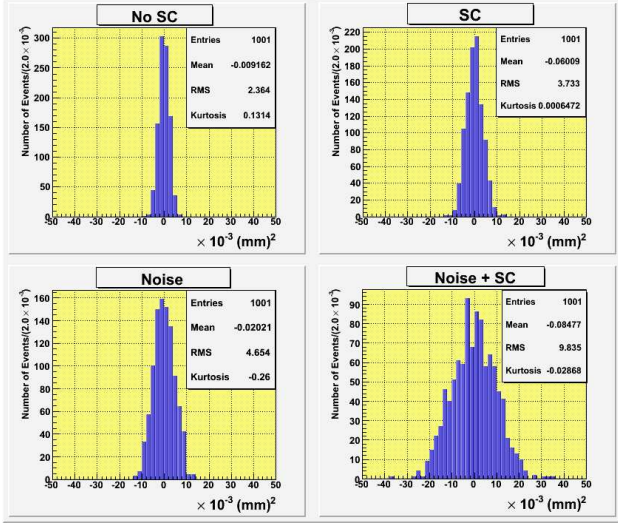


Figure 19 | Distributions of the magnitude of the 2nd-order cross-moment ($\langle xy \rangle$).

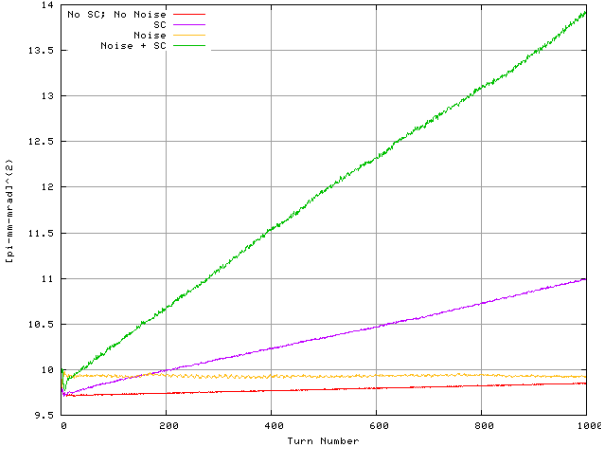


Figure 20 | Time evolution of 4-dimensional coupling strength $\Delta\epsilon_{xy}^4$. Its vertical axis is in units of π -mm-mrad².

the differential-mode voltage at each individual GMPS is well-smoothed with the aid of a 15-Hz low-pass filter installed in each GMPS unit. As found with careful diagnosis, the existent common-mode voltages at each GMPS unit are the principal culprit that triggers ripple currents. As a result of characterising the power-supply noise with the three parameters — *i.e.*, *time step*, *autocorrelation time*, and *noise strength*— its FFT power-spectral densities between the measured ripples and simulated O-U noise are closely matched. The foregoing results from simulating and tracking beams, whilst measurement-based magnetic-field fluctuations induced by the ripples, make evident that non-white noise originating from the power supplies in the face of space charge leads to decidedly heightened beam-degrading process —*i.e.*, emittance growth, halo formation, particle losses, and radiation damage—at the low injection energy of the Booster. Our investigations evidenced that the adverse effects of the power-supply minute ripples are de-

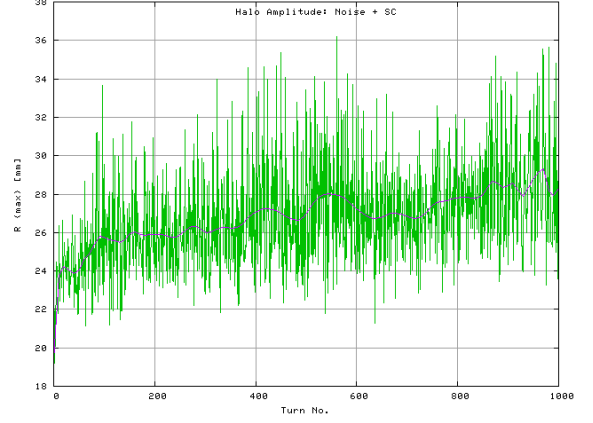


Figure 21 | Halo magnitudes R_{max} with the GMPS noise in the presence of the full space-charge forces; the blue trace in the background indicates a smoothed curve with the spline function.

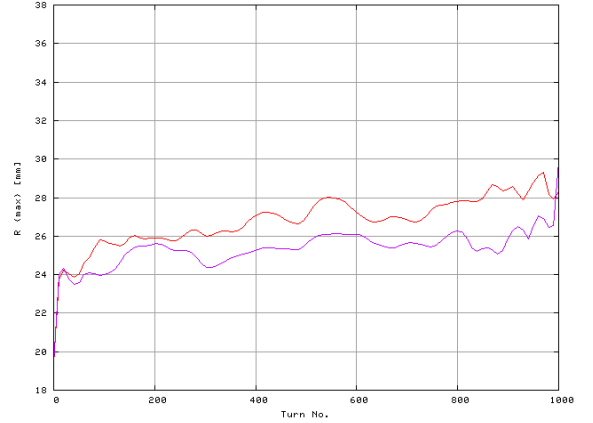


Figure 22 | Halo magnitudes R_{max} in the presence of the GMPS noise along with the full space-charge forces (red) in contrast to the full space-charge forces alone (blue).

pendent upon the strength of space charge. Therefore, as a relevant side, we are proposing two approaches to coping with the adverse impact that the ripples have on intense beams under self-fields: The first is to debilitate inherent space-charge forces themselves. Over the past decades, the efforts have been made to mitigate the space-charge effects arising from the accelerator system of Fermilab, whilst the Booster have endured throughout. For instance, in 1993 Fermilab's proton linac was upgraded from a beam kinetic energy of 200 MeV to 400 MeV by adding more klystron tanks, so as to reduce the space-charge effects during the Booster operation. Besides, a dual radio-frequency (RF) system with a proper choice of RF parameters, allows us to further reduce space-charge effects in high-intensity proton machines by maneuvering charge distributions in longitudinal space [6]. Consequently, one can suppress resultant phenomena of degrading beam properties that are induced by coexisting fluctuational currents and space charge. The second is to devise instrumental techniques to counterbalance common-mode-

conducted EMI originating from the power supplies. In particular, as demonstrated by the equivalent-circuit model, experimental measurements, or detection of harmful high-frequency resonances existent in the magnet system is worth pursuing (Figure 11). Once confirmed, a cluster of parasitic high-frequency resonances makes its presence experienced all around the Booster ring. It is, therefore, required to damp out those offending resonances, such that their adverse influence on beams can be counteracted and insulated from amplifying. Upon including even more realistic, or *nonuniform* charge-density distributions, the effects of space charge increases, so does the damaging influence of meager current fluctuations on the Booster beams. The modelling methodology presented in this paper is expected to be well applicable to other synchrotrons, or storage rings, in which space-charge effects are of main concern. This conclusion is an implication that power-supply ripple currents can induce more prominent development of beam-degrading process in low- γ storage rings of intensity frontier over longer period of time.

- [1] Bohn, C. L. & Sideris, I. V., *Fluctuations Do Matter: Large Noise-Enhanced Halos in Charged-Particle Beams*. Phys. Rev. Lett., **91**, 26, (2003).
- [2] Bohn, C. L., *Collective Modes and Colored Noise as Beam Halo Amplifiers*. AIP Conf. Proc., **737**, 456—461, (2004).
- [3] Galambos, J., *ORBIT—A Ring Injection Code With Space Charge*. Proc. of Particle Accelerator Conference, New York, (1999).
- [4] Uhlenbeck, G. E. & Ornstein, L. S., *ON THE THEORY OF THE BROWNIAN MOTION*. Phys. Rev., **36**, 823, (1930).
- [5] Van Kampen, N. G., *Stochastic Processes in Physics and Chemistry*. (North-Holland, 1992).
- [6] P. S. Yoon, D. E. Johnson, and W. Chou *The Modeling of Microbunch Injection into the Main Injector* arXiv:0802.2430v1 [physics.acc-ph], Fermilab-TM-2368-AD-APC, 2008.
- [7] N. Mohan, T. Undeland, and R. Robbins, *Power Electronics*, John Wiley & Sons, 500—501, 1989.
- [8] P. Horowitz and W. Hill, *The Art of Electronics*, Cambridge University Press, 1989.
- [9] A. Einstein and L. Hopf, *Statistische Untersuchung der Bewegung eines Resonators in einem Strahlungsfeld*, Ann. d. Phys. (Leipzig), **33**, 1105, 1910.
- [10] A. Einstein, R. H. Fürth Ed. *Investigations on the Theory of Brownian Movement*, Methuen, London, 1926, Dover Publication, New York, 1956
- [11] P. Langevin, *Sur la Théorie du motion de brownien*, Comptes Rendus Acad. Sci. (Paris), **146**, 1908, pp. 530—533
- [12] M. Jannesai et al. *A Langevin equation that governs the irregular stick-slip nano-scale friction*, Sci. Rep. (2019) 9:12505.
- [13] G. I. Taylor, *Proc. London Math. Soc.* **22**, 196 (1920)
- [14] J. L. Doob, *The Brownian Movement and Stochastic Equation*, Annals of Mathematics, **43**, 2, 1942, pp. 351—369
- [15] M. G. Wang and G. E. Uhlenbeck, *On the Theory of the Brownian Motion II*, Rev. Mod. Phys. **17**, 2—3, 1945, pp. 323—342
- [16] G. E. P. Box and M. E. Muller, *A Note on the Generation of Random Normal Deviates*, Annals Math. Stat., **29**, 2, 1958, pp. 610—611
- [17] W. H. Press, B. P. Flannery, S. A. Teukolsky, *Numerical Recipes in C++*, (Cambridge University, Cambridge, 1998), pp. 292—293
- [18] Courtesy of M. Kufer and S. Fang of Fermilab Accelerator Division Electrical Engineering Department
- [19] J. Engelbert, T. Nguyen and C. Thurston, *B2 Spice A/D Version 4 User's Manual*, Beige Bag Software, Inc., 2002
- [20] J. Galambos et al., *Comparison of Simulated and Observed Beam Profile Broadening in the Proton Storage Ring and the Role of Space Charge*, PRST-AB, **3**, 034201, 2000
- [21] Kwang-Je Kim, *Round-to-Flat Transformation of Angular-Momentum-Dominated Beam*, Phys. Rev. Spec. Top. Accel. Beams, **6**, 104002, 2003.
- [22] MAD 8 home page: <http://hansg.home.cern.ch/hansg/mad/mad8/mad8.html>
- [23] M. Reiser, *Theory of Charged Particle Beams*, Wiley & Sons, 1994.
- [24] W. Gardiner, *Handbook of Stochastic Processes*, Springer-Verlag, 2004.
- [25] R. L. Stratonovich, *Introduction to the Theory of Random Noise, Vol. I and II*, Gordon and Breach, New York, 1963.
- [26] J. Struckmeier, *Stochastic effects in real and simulated charged particle beams*, Phys. Rev. Spec. Top. Accel. Beams, **13**, (2010).
- [27] Fermilab Lattice Quantum Chromodynamics (QCD) home page, <http://lqcd.fnal.gov>